PAPER

Check for updates

High-energy manganese-rich rocksalt cathodes with engineered oxygen vacancies

Bosu Babu Dasari [ID] and Guoying Chen [ID] *

Manganese-rich (Mn > 0.6) disordered rocksalt (DRX) cathodes undergo structural transformation into a spinel-like δ-phase upon cycling, resulting in enhanced energy density and cycling stability. This transformation is a gradual process, often requiring tens of cycles, which presents challenges in their practical implementation. Here, we synthesized a fluorine-containing, d^0 transition-metal (TM)-free, Mn-rich DRX with oxygen vacancies ($Li_{1.1}Mn_{0.9}O_{1.8-z}F_{0.2}$, OV-M90) and investigated the roles of lithium and oxygen non-stoichiometry, redox reactions, and Mn migration in the DRX-to-δ transformation. We found that the tetrahedral site activation, critical for δ-phase formation, is promoted by synergistic interactions among these factors. A CCCV protocol at 50 °C enables rapid δ-phase activation within a single cycle. While d^0 TM dopants slow the transformation, they substantially improve the cycling stability. The Ti and Al co-doped $Li_{1.05}Mn_{0.85}Ti_{0.05}Al_{0.05}O_{1.8-z}F_{0.1}$ (OV-M85T5A5) maintains nearly 100% capacity retention over 100 cycles at 30 mA g^{-1}. These findings provide insights into the DRX-to-δ transformation mechanism and present strategies to overcome the kinetic limitations while improving the cycling stability, paving the way for the development of cost-effective, high-energy cathodes for next-generation lithium-ion batteries.

Broader context

The global deployment of lithium-ion batteries for electric vehicles and grid-scale energy storage faces critical sustainability challenges due to its reliance on cobalt and nickel materials with severe environmental, ethical, and supply chain vulnerabilities. Disordered rocksalt (DRX) cathodes offer a transformative solution by enabling the use of earth-abundant elements such as manganese (Mn) as primary redox-active species, eliminating the dependence on problematic critical materials while maintaining competitive energy densities. However, high-Mn DRX cathodes face a key barrier: the beneficial structural transformation to a high-performance spinel-like δ-phase typically requires tens of cycles for activation, hindering practical implementation. This study directly addresses this limitation by systematically elucidating the complex mechanisms governing the DRX-to-δ transformation, including the synergistic roles of lithium vacancies, oxygen vacancies, redox processes, and manganese migration. Through this understanding, we demonstrate breakthrough activation strategies that achieve rapid δ-phase transformation within a single cycle using an innovative CCCV protocol at 50 °C. Furthermore, our Ti/Al co-doped compositions exhibit exceptional long-term stability with nearly 100% capacity retention over extended cycling. These advances establish viable pathways toward cobalt- and nickel-free cathodes that satisfy the stringent performance, scalability, and sustainability requirements essential for next-generation energy storage systems.

Introduction

The challenge of meeting the growing demand for lithium-ion batteries (LIBs) for energy storage is compounded by the high cost and supply chain issues associated with cobalt (Co) and nickel (Ni) used in current cathode materials. To address this, alternative Ni- and Co-free chemistries are being explored.[1,2] Recently, manganese (Mn)-containing disordered rocksalt (DRX) cathode materials have garnered great research attention due to their earth-abundant compositions, structural flexi-

bility, and high energy densities.[3,4] DRX oxides, such as $Li_{1+x}Mn_yM'_{1-x-y}O_2$ (where M′ = Ti and Nb), rely heavily on oxygen redox, which leads to rapid capacity fade. To suppress the negative impact of irreversible oxygen redox and enhance electrochemical stability, several approaches have been investigated. Huang et al. showed that substituting the labile oxygen in the Li–O–Li configurations with oxygen vacancies (OV) is an effective strategy to inhibit oxygen oxidation.[5–7] The OV-containing Mn-DRX oxide cathode was found to exhibit increased transition-metal (TM) redox and decreased O-oxidation, with consequently improved capacity and voltage retention. Fluorination was also developed as an effective mitigating strategy, with $Li_{1+x}Mn_yM'_{1-x-y}O_{1-z}F_z$ oxyfluoride cathodes generally exhibiting reduced oxygen gas evolution and improved

Energy Storage and Distributed Resources Division, Lawrence Berkeley National Laboratory, Berkeley, CA 94720, USA. E-mail: gchen@lbl.gov

high-voltage, surface, and cycling stabilities.[8–11] The combined effect of OV and fluorination on DRX, however, has not yet been investigated.

Upon increasing the Mn content to above 0.6, Mn-rich $Li_{1+x}Mn_yM'_{1-x-y}O_{1-z}F_z$ cathodes undergo a pseudo-topotactical phase transition during electrochemical cycling, transforming from the parent cation-disordered structure to a partially disordered "spinel-like" phase known as the δ-phase.[12] Our recent work demonstrated that the DRX-to-δ phase transformation primarily occurs during delithiation and relithiation at the high state-of-charge (SOC), where structural transformation is facilitated by the low Li content.[13] The process offers several advantages, including enhanced energy density and cycling stability,[8,13–17] which is in stark contrast to the layered-to-spinel transformation observed upon cycling of the lithium- and Mn-rich (LMR) cathodes. In the LMR case, the loss of lithium and oxygen destabilizes the layered lattice and leads to the formation of a Li-poor ordered $LiMn_2O_4$-type spinel phase ($Fd\bar{3}m$), resulting in voltage decay.[18–20] It is well known that in the ordered spinels, lithium occupies $1/8^{th}$ of the tetrahedral (8a) sites while Mn occupies half of the octahedral (O_h) (16d) sites, with lithium diffusing through the vacant 16c sites. The spinel structure typically lithiates with two distinct voltage plateaus around 4 V and 3 V, corresponding to lithium occupancy in the 8a and 16c sites, respectively, which provide nearly equal capacity contributions with a theoretical capacity of 295 mA h g^{-1}. Due to the irreversible phase transition from the cubic spinel to a tetragonal phase, utilizing the 3 V plateau leads to poor capacity retention in the spinel or LMR cathodes.[21] On the other hand, the presence of partial ordering in the δ-phase, with some Mn ions occupying the 16c sites (instead of 16d) and face-sharing with the Li-occupied 8a sites, leads to unique voltage profiles without the distinct voltage plateaus. The high-energy atomic arrangement restricts full Li occupancy at the 8a sites, resulting in lower capacity at the sloping 4 V plateau region compared with that of the 3 V plateau region, and solid solution behavior in the 3 V region, which becomes highly reversible.[17,22]

It has been reported that the DRX-to-δ phase transformation is a gradual process and the activation typically takes tens of cycles (even at low current densities),[2,16,23] which is challenging to accommodate in commercial applications. Recently, Holstun et al. reported an electrochemical pulsing method to achieve fast activation of the δ-phase in large DRX crystals.[24] However, understanding the origin behind the δ-phase formation, the factors influencing the transformation and its cycling performance are still lacking. Here, we synthesized an OV-containing and d^0-TM-free DRX oxyfluoride with ultra-high Mn content ($Li_{1.1}Mn_{0.9}O_{1.8-z}F_{0.2}$, OV-M90) for the first time to investigate the roles of Li and O vacancies, Mn migration, and d^0 TM in redox reactions. While earlier studies suggested that the presence of a d^0-TM (such as Ti^{4+} and Nb^{5+}) is essential for δ-phase formation,[17,25] we have shown that the DRX-to-δ transformation is primarily governed by the Mn content, regardless of the presence of a d^0 TM or its content. We have further revealed that the vacancies

generated at high SOC play a key role in δ-phase activation and the 4 V lithiation process. Kinetic factors, including current density (CD), temperature, and overpotential, are evaluated for their roles in δ-phase activation. d^0 TM dopants such as Ti and Al were found to greatly improve the stability of the 3 V process, revealing their key role in influencing the cooperative Jahn–Teller distortion of the Mn^{3+} O_6 octahedra.[26,27] While the presence of d^0 TM decelerates the δ transformation process, it significantly enhances the cycling stability of the δ-activated DRX, with the Ti and Al co-doped $Li_{1.05}Mn_{0.85}Ti_{0.05}Al_{0.05}O_{1.8-z}F_{0.1}$ (OV-M85T5A5) achieving nearly 100% capacity retention after 100 cycles at 30 mA g^{-1}. Our study provides critical insights into accelerating the δ-phase activation and improving its stability, offering a pathway to overcome the kinetic limitations and realize the practical applicability of DRX cathodes in next-generation LIBs.

Results and discussion

Synthesis and properties of OV-M90

The synthesis of phase-pure ultrahigh-Mn DRX (Mn > 0.8) oxyfluorides presents a significant challenge using conventional solid-state methods. At high temperatures, the reactions often suffer the loss of F and/or Li, leading to the formation of a variety of impurities. Here, $Li_{1.1}Mn_{0.9}O_{1.8-z}F_{0.2}$ was synthesized using a solid-state method followed by high-energy ball milling with a carbon additive, which is part of the standard DRX electrode fabrication process. In the solid-state synthesis, high-temperature reactions at 1050 °C in an argon (Ar) atmosphere are known to promote the loss of lattice oxygen,[28–30] leading to the formation of a phase-pure fluorinated orthorhombic phase with oxygen vacancies (OV-M90-O, SG: Pmmn). This is evidenced by the asymmetry in the diffraction peak intensities of the 110, 111, 210, and 211 planes in the synchrotron X-ray diffraction (XRD) pattern (Fig. 1a, black color),[31] compared with that of the stoichiometric orthorhombic structure (M90-O, SG: Pmmn) prepared at ~800 °C (Fig. 1a, green color). The subsequent ball-milling process during the electrode fabrication process leads to the structural transformation to the DRX phase with OVs (OV-M90, $Fm\bar{3}m$), along with a reduction in crystallite size. The transformation was characterized by the disappearance of ordered reflections and the emergence of broadened Bragg peaks, indicating cation randomization (Fig. 1a, orange color). Atomic-scale models (Fig. 1b–d) further illustrate the structural evolution from the cation-ordered arrangements in the orthorhombic phase to an OV-containing ordered orthorhombic phase, and finally to a cation-disordered DRX phase with OVs. In the DRX configuration, oxygen and fluorine anions form a face-centered cubic (fcc) lattice at the 4b sites (32e in spinel notation), whereas the lithium and manganese cations are randomly distributed at the 4a sites (16c and 16d in spinel notation) with edge-sharing O_h coordination.[32] Scanning electron microscopy (SEM) images (Fig. 1e and f) reveal a particle size reduction from
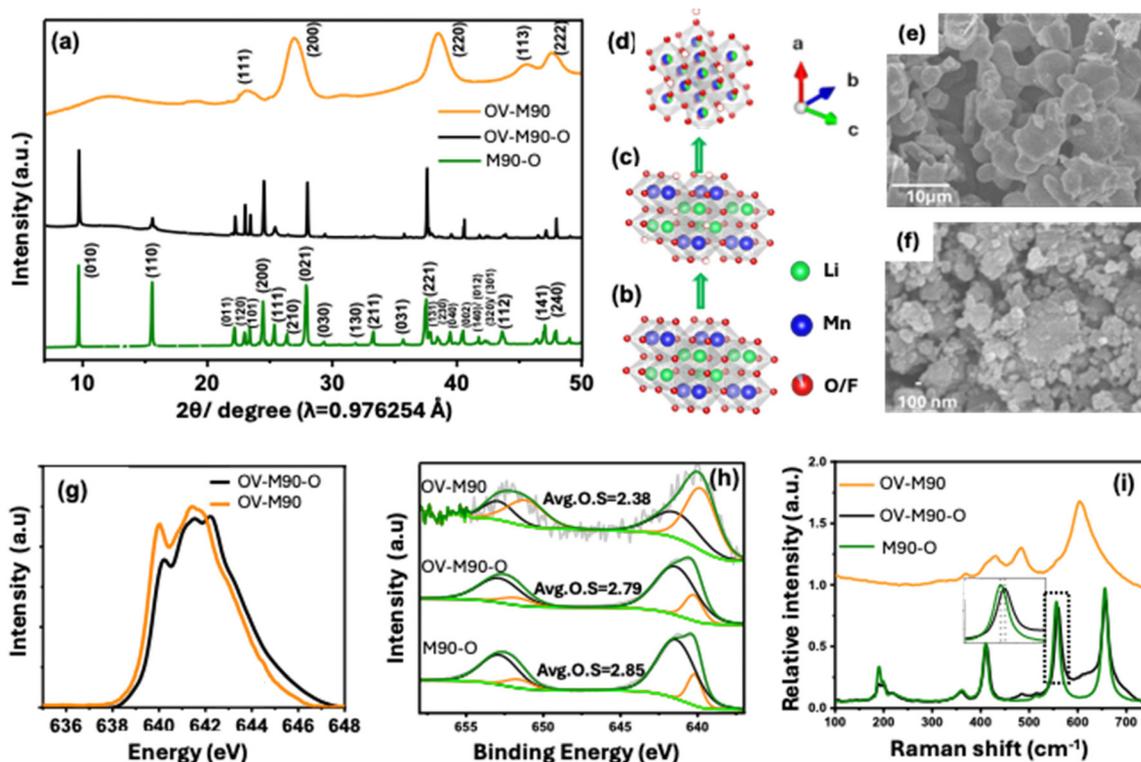
Fig. 1 (a) Synchrotron XRD patterns of the M90-O, OV-M90-O and ball-milled OV-M90 DRX cathodes. (b–d) Atomic structure models depicting the ordering transition from the orthorhombic phase to the DRX phase. SEM images of OV-M90-O (e) and OV-M90 DRX (f). (g–i) TEY Mn L-edge XAS, Mn 2p XPS, and Raman spectra of the as-synthesized samples, respectively.

10 μm to ~100 nm after ball milling, confirming both structural and morphological transformation during the process. The Li : Mn ratio in all samples was verified by inductively coupled plasma mass spectrometry (ICP-MS) analysis. We note that F is included following established Mn-rich DRX 'oxyfluoride/fluorine-containing' formulations reported previously.[8–11] F speciation (lattice-substituted *vs.* surface/secondary fluoride) is beyond the scope of this study.

Soft X-ray absorption spectroscopy (sXAS) data, collected in the total electron yield (TEY, ~5 nm probing depth) mode at the Mn L-edge, oxygen K-edge, and fluorine K-edge, provide detailed insights into the local electronic structure of the samples. The Mn L-edge spectrum (Fig. 1g) indicates a reduced Mn oxidation state in OV-M90-O, which is further corroborated by XPS analysis (Fig. 1h). The results reveal an average Mn oxidation state of 2.79 on the surface, as compared with 2.85 for M90-O. This reduction is consistent with the presence of surface OVs. After ball milling, a pronounced peak near ~640 eV in the Mn L-edge spectrum of OV-M90 highlights the increase in surface Mn^{2+} species (Fig. 1g). Corresponding XPS data (Fig. 1h, OV-M90) reveal a further decrease in the average Mn oxidation state to 2.38, largely attributed to milling-induced oxygen loss and increased OV concentration in the final OV-DRX. Additionally, shifts observed in the oxygen K-edge spectra (Fig. S1a) reflect increased anionic sublattice disordering while maintaining

the structural integrity of the close-packed oxygen framework in OV-M90. The F K-edge, on the other hand, remains mostly unchanged in both samples (Fig. S1b). Raman spectroscopy, a technique sensitive to short-range order, further validates the presence of structural defects and local disorder in the OV-M90 phase (Fig. 1i). A slight blue shift (556 to 559.4 cm^{-1}) and broadening of the 556 cm^{-1} peak can be attributed to OV-induced lattice distortions, as shown in previous studies.[33–35]

We note that direct quantification of oxygen site occupancy through Rietveld refinement was not performed in this study due to the limited sensitivity of X-ray diffraction to oxygen positions in the presence of heavy Mn scatterers, particularly in the nanocrystalline ball-milled DRX phase. We therefore rely on multiple complementary indicators of oxygen deficiency: (i) the synthesis was conducted at 1050 °C under Ar, conditions well-established to promote oxygen loss in lithium manganese oxides; (ii) Mn L-edge XAS and XPS consistently show reduced Mn oxidation states (+2.79 in OV-M90-O *vs.* +2.85 in M90-O), below the +3 expected for stoichiometric compositions; (iii) Raman spectroscopy reveals peak broadening and blue-shifts consistent with lattice distortion from oxygen non-stoichiometry. While we cannot exclude the possibility that some degree of metal densification accompanies the oxygen loss, the totality of the spectroscopic evidence supports sub-stoichiometric oxygen content in these materials.

Understanding δ-phase activation in OV-M90

The electrochemical performance of the OV-M90 cathode was investigated using room-temperature (RT) galvanostatic cycling at 30 mA g^{-1} with upper cutoff voltages (UCVs) of 4.0 V, 4.2 V, 4.4 V, 4.6 V, and 4.8 V, while maintaining the lower cutoff voltage (LCV) at 2.0 V. The 1st cycle voltage profiles (Fig. 2a) show that, at a UCV of 4.4 V, a flat charge plateau emerges, accompanied by a flattening of the 3 V discharge plateau, increased capacity, and increased polarization. The corresponding 1st cycle differential capacity dQ/dV profiles (Fig. S2a) show the appearance of a new broad peak when charged to a UCV of ≥4.4 V, which can be attributed to oxygen oxidation in Li-excess cathodes based on previous studies.[36,37] The peak is much broader, with significantly lower intensity compared with those of the previously reported DRX cathodes, confirming overall lower O activity levels.[16] This was further supported by gas analysis using *operando* differential electrochemical mass spectrometry (DEMS) that directly measures oxygen gas evolution during charge and discharge. We found negligible oxygen loss during the first two cycles of DEMS measurement between 2 and 4.6 V (Fig. S2b), which is consistent with previous reports on OV-containing DRX and fluorinated DRX with a high Mn content.[16,23,38,39] In addition to lower O redox activities in OV-M90, we believe the presence of oxygen vacancies and fluorine further stabilizes the anionic framework, lessening the tendency of O release from the lattice upon oxidation. For example, oxygen vacancies can reduce surface oxygen partial pressure and decrease the density of states of the O 2p band, effectively suppressing surface oxygen loss. We note that the DEMS analysis monitors O_2 evolution only. Given the presence of carbon in the composite electrode, oxygen evolved from the cathode surface may react with carbon to form CO/CO_2. Therefore, while negligible O_2 release was observed, we cannot exclude the possibility of oxygen loss *via* CO_2 evolution. Future studies with CO_2 monitoring will clarify the extent of total oxygen release.

Fig. 2b and Fig. S3 compare the cycling performance of OV-M90 when charged and discharged in various voltage windows. At 2–4.0 V, there is no change in the voltage profiles after the 1st cycle (Fig. S3a), consistent with the high stability of TM redox in this regime. The cell delivered a low 1st cycle discharge capacity and energy of 68 mA h g^{-1} and 180 W h kg^{-1}, respectively, which increased to 76 mA h g^{-1} and 220 W h kg^{-1} after 100 cycles. When increasing the UCV to 4.4 V, where oxygen activation is observed, a rapid increase in discharge capacity is also observed, along with the appearance of strong pseudo-plateaus in both the 4 V and 3 V regions of the discharge curve (Fig. S3c). These features are associated with the formation of the δ-phase, as reported previously.[24,40] The capacity contribution from both regions progressively increases with increasing UCV (Fig. S3d and e). The total discharge capacities increased from 85, 97, 172, and 204 mA h g^{-1} at the 1st cycle to 135, 152, 201, and 214 mA h g^{-1} at the 100th cycle for 2–4.2 V, 2–4.4 V, 2–4.6 V, and 2–4.8 V, respectively, corresponding to a capacity retention of 159%, 157%, 117%, and 105%. Cycling to an LCV below 2 V greatly reduces the stability, with the cell cycling between 1.5 and 4.8 V achieving a capacity retention of 58%, decreasing from 255 mA h g^{-1} at the 1st cycle to 147 mA h g^{-1} at the 100th cycle (Fig. S3f).

The broad peak appearing in the dQ/dV profile during the first cycle (Fig. S2a) disappears in subsequent cycles. This
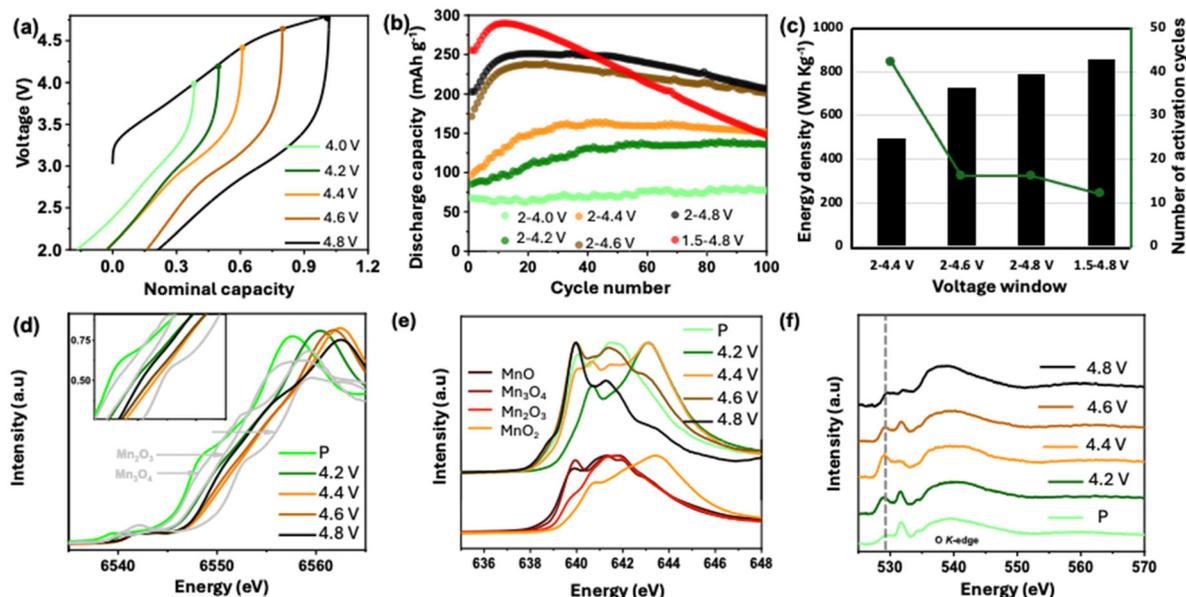

Fig. 2 (a–c) 1st cycle voltage profile, discharge capacity, and number of activation cycles of OV-M90 cathode cycled to various upper cutoff voltages, respectively. (d–f) XANES spectra, FY Mn L-edge and O K-edge XAS profiles of the OV-M90 cathodes at the pristine (P) and various charged states in the first cycle, respectively.

suggests oxygen activation occurs when the upper cutoff voltage is increased to 4.4 V upon initial cycling. The features of the δ-phase emerge concurrently with this oxygen activation peak, and their intensities are directly correlated. This strong correlation indicates that the δ-phase activation is closely linked to oxygen activity during the initial cycling. The number of cycles required to achieve full activation of the δ-phase (when the maximum capacity is reached)[17,24,40,41] is 58, 42, 16, 16, and 12 for 2–4.2 V, 2–4.4 V, 2–4.6 V, 2–4.8 V, and 1.5–4.8 V, respectively (Fig. 2c), indicating a faster and more complete formation of δ-phase when cycled to higher voltages where more oxygen activation is involved. Fig. S3g and h further compares the average cell voltage and maximum energy density achieved by the cells. The highest energy density (850 W h kg^{-1}) was achieved when cycled between 1.5 and 4.8 V. The cells cycled to 4.6 V and 4.8 V achieved 725 and 790 W h kg^{-1}, respectively, with an average of ~3.15 V. Considering the increasing impact of parasitic reactions at higher voltages and the lower capacity retention of the 1.5–4.8 V cell, the voltage window of 2–4.6 V was chosen for all subsequent cycling studies.

To understand the changes in bulk electronic structure, *ex situ* Mn K-edge hard X-ray absorption near-edge structure (XANES) spectra were collected on the pristine (P) and cycled OV-M90 samples recovered at voltages of 4.2 V, 4.4 V, 4.6 V, and 4.8 V during the 1st charge (Fig. 2d); various Mn reference spectra were also collected and are shown in the figure. The Mn K-edge position is known to be sensitive to changes in Mn valence. The edge energy of P is close to that of Mn_3O_4, suggesting that the bulk Mn has an average oxidation state of +~2.67. This value is well below +3 expected in stoichiometric M90, further confirming the presence of OV in the sample. Upon charging, the K-edge gradually shifts towards higher energy compared with that in the pristine state, reaching 4.2 V and then 4.4 V, indicating continuous Mn oxidation in the bulk. The maximum edge energy was reached at 4.4 V, which is slightly lower than the +4 in the MnO_2 reference. The changes at 4.6 V are not significant, and the Mn K-edge energy mostly aligns with that of 4.4 V. Further increasing the UCV to 4.8 V leads to a slight reduction in Mn oxidation state. The evolution trend in the pre-peak position and intensity is also consistent with these observations (Fig. S4a). These results suggest that the additional capacity obtained above 4.4 V is charge compensated by the removal of electrons from oxygen 2p orbitals.[42,43] Electrons are transferred from the oxygen ligand to the Mn orbitals, leading to Mn reduction and stabilization of the oxidized oxygen species through stronger Mn–O bonding, known as the LMCT process.[17,39,44,45] The stronger bonding likely contributed to the broad feature of the peak above 4.4 V on the dQ/dV profile and negligible O_2 release in the DEMS measurements. At 4.8 V, side reactions with the electrolyte become significant, as shown in the sXAS analysis in the following section, which can also contribute to Mn reduction.

Fig. 2e shows the *ex situ* sXAS profiles of Mn L-edge collected in the total fluorescence yield (FY, ~50 nm probing depth) mode. Various Mn reference spectra of +2, +2.67, +3, and +4 were also collected and are shown in the figure. At 4.2

V, the Mn oxidation state increases from the pristine, as indicated by the intensity shift toward the higher energy peak (~644 eV) consistent with higher Mn^{4+} contribution. Upon charging to 4.4 V, the Mn L-edge exhibits a low-energy shift, corresponding to a decrease in the concentration of Mn^{4+} and an increase in the concentrations of Mn^{3+} and Mn^{2+}. The surface reduction of Mn continues at 4.6 V and 4.8 V. These results were further confirmed by XPS analysis (Fig. S4b), where Mn is oxidized from 2.38 (pristine) to 3.54 (4.2 V), as evidenced by the presence of the 643 eV peak, followed by a reduction to 2.58 at 4.6 V with the dominance of Mn^{2+}, pointing to significant surface reduction.

The corresponding *ex situ* FY sXAS profiles of the O K-edge (Fig. 2f) exhibit two distinct regions: the pre-edge region (529–532 eV) and the higher-energy region (535–550 eV), corresponding to electron transitions from O 1s to the hybridized Mn 3d–O 2p and Mn 4s/4p–O 2p orbitals, respectively.[46,47] Compared with the pristine state, a noticeable increase of the pre-edge peak at 529 eV (dashed line in Fig. 2f) was observed at 4.2 V, indicating the formation of additional empty states caused by the oxidation of Mn. This creates more holes in the 2p–3d hybrid orbitals. An increase in the density of these empty states is observed from 4.2 to 4.4 V, with the intensity of the 529 eV peak being significantly higher at 4.4 V, implying enhanced Mn 3d–O 2p hybridization and stronger Mn–O covalent interactions. As the corresponding Mn L-edge sXAS profiles (Fig. 2d) show a lower Mn oxidation state at 4.4 V, the additional intensity of the 529 eV peak and unoccupied states at 4.4 V can be attributed to the removal of electrons from oxygen 2p orbitals.[42,43] This is consistent with the electrochemical analysis, where O redox contributes to charge compensation at 4.4 V. A similar evolution in the intensity of the 529 eV and 532 eV peaks was also observed in the top surface region, as shown in the O K-edge profiles collected in the TEY mode (Fig. S4c). The intensity of the 529 eV peak, however, appears much diminished compared with that of the corresponding FY spectrum. This is likely due to the stronger interaction with the electrolyte on the top surface and enhanced parasitic reactions at higher voltages.

Fig. 3 shows schematics illustrating the proposed mechanism of initiating the DRX-to-δ phase transformation process during the initial cycles. When charged to a UCV below 4.4 V, lithium extraction in OV-M90 is predominantly achieved through Mn oxidation, leading to the presence of lithium vacancies on top of the preexisting O vacancies in the lattice (Fig. 3a and b). Charging to a UCV of ≥4.4 V activates the oxygen oxidation, enabling the extraction of additional Li and a higher Li vacancy concentration (Fig. 3b and c). The lack of O_2 evolution in the DEMS results suggests that the oxidized oxygen mainly remains in the lattice, rather than creating additional O vacancies, partly due to the presence of the preexisting O vacancies in the lattice. The high density of Li vacancies triggers Mn migration and T_d (8a) site activation, leading to the formation of a spinel-like phase or δ-phase (Fig. 3c). Further increasing the charging voltage promotes more oxygen participation and a higher density of Li vacancies,
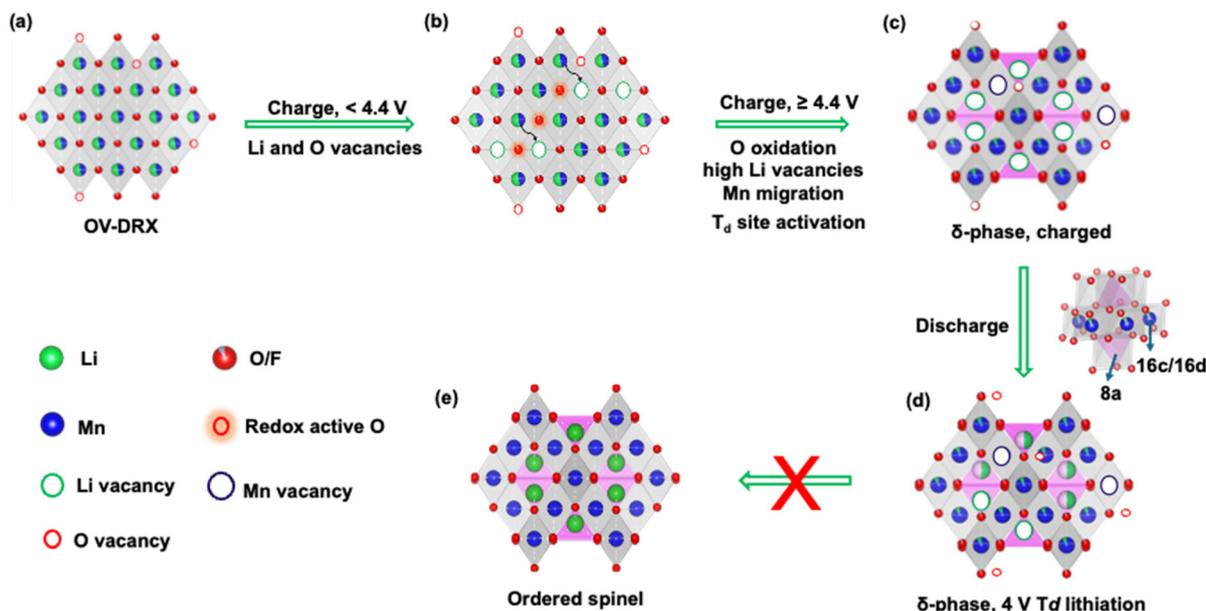
Fig. 3 Schematics of the proposed DRX-to-δ transformation during cycling: (a,b) delithiation below 4.4 V dominated by Mn redox, generating Li vacancies in OV-DRX; (c) delithiation ≥4.4 V activates oxygen redox, increases Li-vacancy concentration, and promotes Mn migration and Td (8a) activation to form the δ phase; (d) δ phase showing Li insertion into Td sites; (e) comparison with ordered spinel highlighting restricted 8a-site utilization in δ.

accelerating δ formation. Furthermore, increased surface Mn reduction above 4.6 V generates mobile Mn^{2+} and Mn^{3+} species with lower migration barriers, further accelerating Mn migration into the lithium vacancy sites ($16c/16d$ O_h sites) and promoting δ-phase transformation. This is consistent with the observation that the activation cycle number decreases from 42 to 16 when increasing the UCV from 4.4 to 4.8 V (Fig. 2c).

The atomic arrangement in the delithiated δ-phase activates a new Li transport pathway (T_d sites), as evidenced by the voltage plateaus, which are distinctly different from the sloped charge/discharge profiles typically observed in low-Mn DRX materials. Similar to the ordered $LiMn_2O_4$ spinels, Li insertion into the δ-phase occurs in two stages: 4 V ($8a$ site) and 3 V ($16d$ site). However, the initial lithiation in the T_d sites plays a major role in the δ-phase. This is because the complete activation of the $8a$ sites is restricted as they face-share with Mn ions in the $16c$ sites (Fig. 3d). This high-energy configuration introduces kinetic limitations, restricting full lithium occupancy in the 4 V region, resulting in a lower capacity at the 4 V plateau (~70 mA h g^{-1} in OV-M90) compared with that in the ordered spinels (~140 mA h g^{-1} in $LiMn_2O_4$) (Fig. 3e). This is advantageous as lithiation of $LiMn_2O_4$ goes through a collective two-phase cubic-tetragonal transformation when the full tetrahedral $8a$ site Li occupancy converts to the $16d$ site occupancy. Because of the reduction of Mn to +3, a cooperative Jahn–Teller distortion, where adjacent Mn^{3+}–O_6 octahedra distort in a correlated manner, also occurs. The large strain caused by the non-uniform transformation degrades the material and destabilizes the 3 V region, which limits the usable capacity of fully ordered spinel to the 4 V region

only.[48,49] In contrast, in OV-M90, the average Mn oxidation state is slightly below +3, lowering the concentration of Mn^{3+}. In addition, partial cationic disordering (excess Li at Mn sites and Li/Mn exchange) in the δ phase appears to break the symmetry of Mn^{3+} arrangements, disrupting the correlation of distortions arising from individual JT centers and preventing the Mn^{3+}–O bonds from distorting along one direction, consequently suppressing the CJTD of Mn^{3+} O_6 octahedra, even in the absence of d^0 TM.[50] The collective distortion is reduced, and the two-phase reaction is converted into a solid-solution reaction, improving the stability of the 3 V region. While previous studies showed that the presence of d^0 TM is essential in order to form the DRX phase during synthesis and to promote the DRX-to-δ phase transformation during cycling,[17,24,40,41,51] our study demonstrates that both processes can occur in d^0 TM-free OV-M90 in a similar manner. In addition, the results reveal that the presence of d^0 TM is not essential for preventing the δ-to-spinel transformation in DRX, in contrast to the previous reports based on theoretical studies.[17,24,40,41]

Expediting δ-phase activation

Upon initiation, the apparent slow kinetics of δ-phase activation in OV-M90 is primarily a result of the restricted availability of lithium in the $8a$ sites. The activation of these sites is largely determined by the interplay between the vacancies, including both Li and O vacancies. To this end, we evaluated the parameters that influence vacancy formation kinetics, including current density, temperature and overpotential.
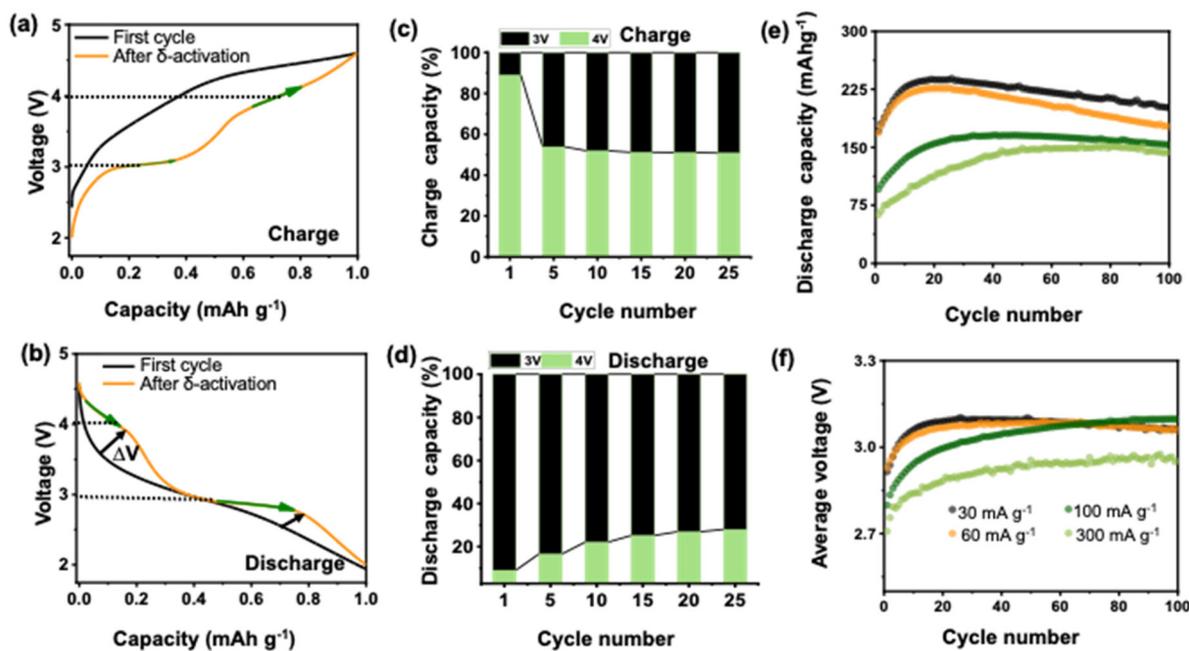
Fig. 4 (a and b) Evolution of the voltage profile upon δ-phase activation during the charge and discharge of OV-M90, respectively. (c and d) Evolution of the 4 V and 3 V capacity contribution upon cycling, shown as charge and discharge, respectively. (e and f) Discharge capacity and average voltage retention when cycled with various current densities, respectively.

Current density. Fig. 4 and Fig. S5 compare the cycling performance of the OV-M90 cathode at four current densities of 30, 60, 100, and 300 mA g^{-1}. The voltage profiles show that, regardless of the current densities, the 4 V and 3 V plateaus continuously evolve in the early cycles, indicating a gradual DRX-to-δ phase transformation upon cycling (Fig. S5a–d and Fig. 4a and b). To better understand the activation process, the charge and discharge capacities obtained in the 4 V and 3 V regions during the first 25 cycles at 30 mA g^{-1} are shown in Fig. 4c and d, respectively. The continuous increase in 4 V discharge capacity percentage indicates that the activation process is predominantly driven by the 4 V region, whereas during charging, both 4 V and 3 V capacities remain largely unchanged after the 1st cycle. The changes occur more rapidly at a lower CD, attaining the maximum capacity within ~15 cycles at a CD of 30 or 60 mA g^{-1}, as opposed to 30 cycles for 100 mA g^{-1} and 50 cycles for 300 mA g^{-1}. At higher current densities, the activation process is significantly prolonged as lithium preferentially inserts into energetically favorable O_h sites, where lower coulombic repulsions facilitate the insertion. In contrast, slower currents promote lithium insertion into the higher energy T_d sites, enabling faster activation and reducing the activation cycle number. Cycling at lower CD not only improves discharge capacity (Fig. 4e), average voltage (Fig. 4f), and energy density (Fig. S5e), but also enhances coulombic efficiency (Fig. S5f). Oxygen redox is known to have slow kinetics[52–54] and its activation is limited at high current densities. The correlation in the absence of an oxygen redox peak in the 1st cycle dQ/dV plots (Fig. S5g) and the higher activation cycle numbers (Fig. S5h) at both 100 and 300 mA g^{-1}

further support the key role of oxygen activation in the DRX-to-δ phase transformation in OV-M90.

Temperature and overpotential. Elevated temperature (ET) and overpotential are well-known parameters for controlling kinetics, enhancing lithium mobility, and expediting sluggish phase transitions. Here, we investigated the effects of ET and a constant voltage (CV) hold at the top-of-charge (TOC) of 4.6 V on δ activation. Four cycling protocols were compared, including room temperature constant current charge and discharge (RT-CC), 50 °C constant current charge and discharge (50-CC), room temperature constant current charge to 4.6 V followed by a constant voltage hold at 4.6 V for 5 h (RT-CCCV), and 50 °C constant current charge to 4.6 V followed by a constant voltage hold at 4.6 V for 5 h (50-CCCV). All constant current was 30 mA g^{-1} and the CC cycling voltage window was 2–4.6 V.

Compared with RT-CC (Fig. 5a), the voltage profiles cycled under 50-CC (Fig. 5b) exhibited significantly improved kinetics, quickly generating a higher concentration of lithium vacancies by enhancing oxygen activation and Mn redox activities. This resulted in a higher initial discharge capacity of 258 mA h g^{-1} as compared with 158 mA h g^{-1} in the RT-CC cell (Fig. S6a), *i.e.*, a 45% improvement. Further confirmation of improved redox kinetics and DRX-to-δ transformation under ET was obtained from dQ/dV analysis (Fig. S6b), in which faster 3 V and 4 V peak evolution and peak shifts under ET cycling are clearly shown. Additional lithium extraction was achieved when a CV hold was added at the TOC (RT-CCCV, Fig. 5c), further promoting vacancy generation and accelerating δ-phase formation. Under 50-CCCV (Fig. 5d), the maximum discharge capacity was nearly fully achieved within
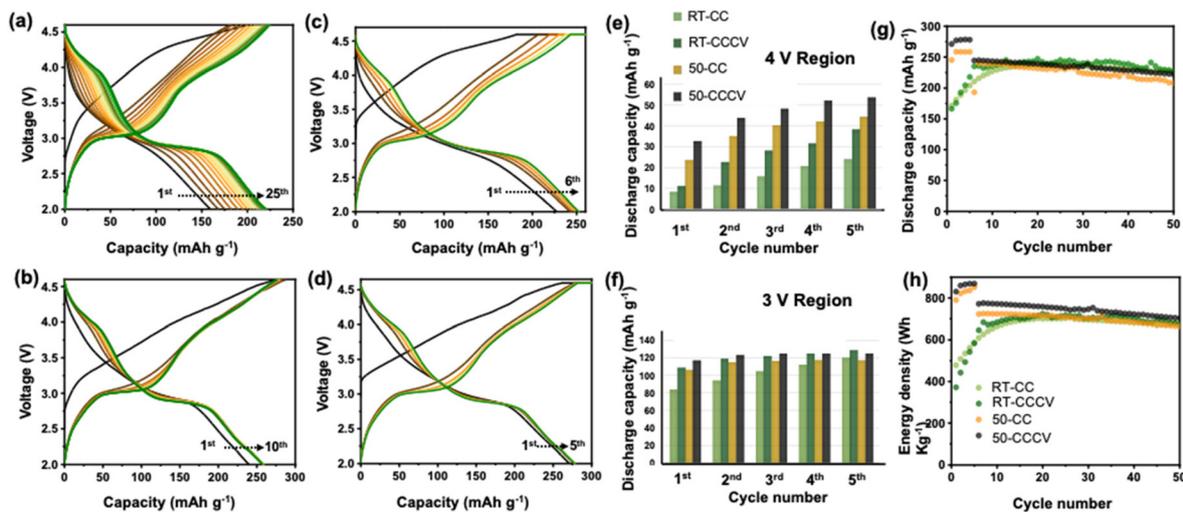
Fig. 5 (a–d) Comparison of voltage profiles of the OV-M90 cathode when cycled with four different cycling protocols: RT-CC, 50-CC, RT-CCCV, and 50-CCCV, respectively. Evolution of discharge capacity contribution from the 4 V (e) and 3 V (f) region, respectively. Discharge capacity retention (g) and energy density retention (h) of the OV-M90 cathode cycled using the various cycling protocols, as indicated.

the first cycle (270 mA h g^{-1}), and only increased slightly in the second cycle (276 mA h g^{-1}). The full capacity of the 4 V discharge region was reached within the first 2 cycles, whereas nearly 10 cycles were required for RT-CC. This highlights that T_d site activation is significantly accelerated under both ET and overpotential conditions. Notably, during the initial charge, the 4 V discharge capacity in 50-CCCV is more than three times higher than that in RT-CC, a trend that persists in the subsequent cycles (Fig. 5e). In contrast, the 3 V region shows moderate capacity increases from RT-CC to RT-CCCV cycling, whereas in the 50-CC and 50-CCCV cycling, the capacity remains nearly unchanged (Fig. 5f). These differences in peak evolution during RT-CC (Fig. S6c–e) and 50-CCCV (Fig. S6f–h) cycling are further shown in the dQ/dV plots. The results suggest that the bottleneck in DRX-to-δ transformation occurs at the 4 V region, and the kinetics can be improved by promoting the 4 V process.

We further evaluated the contribution of oxygen evolution using DEMS analysis (Fig. S7). The results confirm negligible O$_2$ gas evolution under various cycling conditions. Even under 50-CCCV cycling, only a small amount of O$_2$ (~8 μmol g^{-1} min^{-1}) was detected during the first charge, which is significantly lower than the previous results obtained with LMR cathodes such as Li$_{1.17}$[Ni$_{0.22}$Mn$_{0.66}$Co$_{0.12}$]$_{0.83}$O$_2$ and Li$_2$MnO$_3$, where O$_2$ evolution was 30 and 400 times higher, respectively.[55,56]

Despite the fast activation under ET, long-term cycling stability was compromised (Fig. S8). Especially, the 50-CCCV cell retained only about 20% of its original capacity after 50 cycles, exhibiting degradation behavior similar to that of ordered spinel cathodes.[57,58] It is possible that factors such as Mn dissolution play a larger role at elevated temperatures. Side reactions with the electrolyte also present significant challenges at 50 °C. To balance the fast activation of ET while

minimizing degradation, we developed a 50-CCCV/RT-CC cycling protocol where the cells were cycled using the 50-CCCV for the first 5 cycles to achieve the fast DRX-to-δ activation, followed by RT-CC cycling for the rest of the testing. This leads to much improved cycling stability along with fast activation in the first cycle, achieving a discharge capacity of 230 mA h g^{-1} and energy retention of 710 W h kg^{-1} after 50 cycles, with ~90% retention from the maximum values achieved for both. The performances are similar to those of the slow RT-CC activated cells cycled under the RT-CC protocol (Fig. 5g and h).

Stabilizing δ-phase cycling

Cationic disordering in the δ phase helps to suppress the CJTD of Mn^{3+}O$_6$ octahedra and enable the utilization of the 3 V region through the solid-solution process. However, the long-term cycling performance suggests that the 3 V region still exhibits a gradual capacity decay over cycling, which contributes to the low capacity and energy retention. To this end, we investigated the effect of incorporating immobile cation dopants into the disordered structure to further arrest JT distortion and its detrimental effects. The occupancy of cations smaller than Mn^{3+} (0.645 Å), such as Al^{3+} (0.53 Å) and Ti^{4+} (0.60 Å), in certain lattice sites is likely to alter the local energy landscape and further disrupt the cooperative motion of Mn^{3+} and CJTD. This, in turn, may reinforce the structural stability of the δ phase over extended cycling.[50] A series of OV-DRX samples with the same Mn content of ~0.85, including Li$_{1.15}$Mn$_{0.85}$O$_{1.7-z}$F$_{0.3}$ (OV-M85), Li$_{1.08}$Mn$_{0.86}$Ti$_{0.06}$O$_{1.9-z}$F$_{0.1}$ (OV-M86T6), Li$_{1.1}$Mn$_{0.85}$Al$_{0.05}$O$_{1.8-z}$F$_{0.2}$ (OV-M85A5) and Li$_{1.05}$Mn$_{0.85}$Ti$_{0.05}$Al$_{0.05}$O$_{1.95-z}$F$_{0.05}$ (OV-M85T5A5), were synthesized using the same solid-state process to produce the orthorhombic intermediate. Structural analysis using synchrotron XRD (Fig. S9a) confirmed the phase-pure orthorhombic
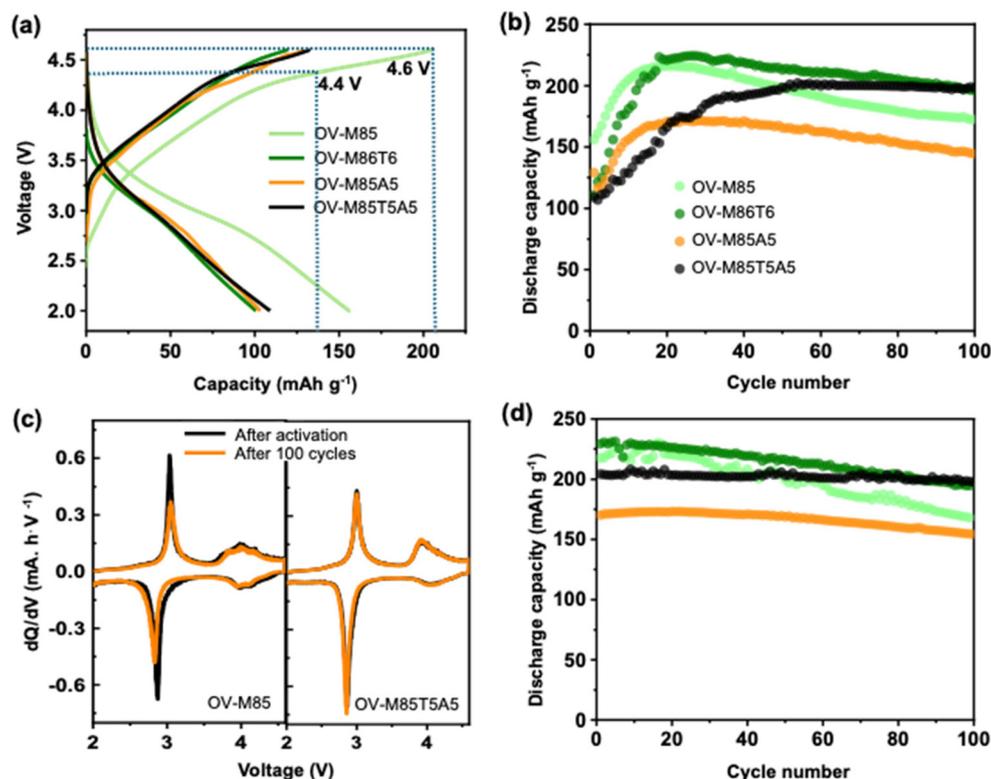
Fig. 6 (a) 1st cycle voltage profiles of the OV-M85, OV-M86T6, OV-M85A5, and OV-M85T5A5 cathodes, (b) discharge capacity of the cathodes during the first 100 cycles using the RT-CC protocol, (c) comparison of the 1st and 100th cycle dQ/dV plots of the OV-M85 and OV-M85T5A5 cathodes, corresponding to the cycling tests shown in (b), and (d) discharge capacity of the cathodes during the first 100 cycles, with the first 5 cycles using the 50-CCCV protocol followed by RT-CC for the rest of the testing. All CC corresponds to 30 mA g^{-1}.

structures. Similarly, the subsequent ball-milling process during electrode fabrication successfully produced homogeneous phase-pure DRX structures (Fig. S9b).

Fig. 6 and Fig. S10 show the cathode performance during RT-CC cycling between 2 and 4.6 V at 30 mA g^{-1}. Compared with the undoped OV-M85, the initial charge profile reveals that the doped compositions exhibit a much lower capacity above 4.4 V (Fig. 6a), suggesting that the dopants suppress the activation of O oxidation. We hypothesize that the improved stability may arise from stronger Al–O and Ti–O bonds relative to Mn–O bonds (Table S1), which could hinder oxygen oxidation and limit vacancy formation. While the specific mechanism requires further investigation, the correlation between dopant presence and improved 3 V region stability (Fig. 6c) supports a role for these cations in suppressing cooperative Jahn–Teller distortions. This leads to a longer activation in the doped samples compared with that of the undoped OV-M85 or OV-M90. As shown in Fig. 6b, the number of cycles for δ-phase activation is roughly 16, 20, 20, and 38 cycles for OV-M85, OV-M86T6, OV-M85A5, and OV-M85T5A5, respectively. Ti-doping enhanced the capacity and cycling stability compared with the undoped OV-M85, whereas Al-doping resulted in lower capacity. While the effect of a single dopant of Ti or Al is limited, the co-doped OV-M85T5A5 exhibited a significant improvement in cycling performance, achieving nearly 100%

capacity retention after 100 cycles. A comparison of the dQ/dV profiles of OV-M85 and OV-M85T5A5 after activation and over extended cycling reveals that the improvement predominantly comes from the 3 V plateau region (Fig. 6c), suggesting that the dopants indeed mitigate the JT distortions and lower lattice strain, consequently stabilizing the 3 V discharge plateau. This provides a clear advantage of δ-phase over the ordered spinels, where the instability of the 3 V plateau renders the capacity unusable. We note that Ti- and Al-doped compositions also differ in fluorine content, which may contribute to the observed differences in electrochemical behavior. Future work in which the dopant and fluorine content are independently varied systematically will be necessary to deconvolute these effects.

Using the 50-CCCV/RT-CC cycling protocol we developed, all samples were activated after the 1st cycle, including the doped samples that showed slower activation at room temperature (Fig. 6d). Excellent performance was achieved on OV-M85T5A5, which delivered a stable discharge capacity of ~210 mA h g^{-1} at 30 mA g^{-1} for over 100 cycles, with nearly 100% capacity retention. Considering the abundance of the component elements and its excellent cycling performance, we believe OV-M85T5A5 is a highly promising cathode material for next-generation low-cost and sustainable high-energy LIBs.

Experimental

Material synthesis and electrode fabrication

The synthesis of OV-M90 was achieved using a solid-state method followed by high-energy ball-milling with a carbon additive, which is a typical part of the DRX electrode fabrication process. The initial ordered oxygen-deficient phase (OV-M90-O) was prepared by combining stoichiometric quantities of Li_2CO_3 (99.0%; ACS reagent), Mn_2O_3 (99.9%; ACS reagent), and LiF (99.85%; Alfa Aesar) using a mortar and pestle. To account for potential lithium loss during heating, a 10% excess of lithium precursor was included. The mixture was then placed in an aluminum boat and calcined at 1050 °C for 12 hours under argon flow, with heating and cooling rates of 5 °C min^{-1}.

To construct the DRX composite cathodes, the as-synthesized OV-M90-O was subjected to planetary ball milling at 400 rpm for 4 hours (PM-200, Retsch) in an argon atmosphere, together with a conductive carbon additive (graphite and Denka carbon black, 1 : 1 wt%) in a weight ratio of 80% OV-M90-O and 20% additive. A slurry mixture of 90 : 10 wt% of the resulting carbon-coated OV-M90 DRX and poly(vinylidene fluoride-co-hexafluoropropylene) (PVDF-HFP) binder dissolved in n-methyl-2-pyrrolidone (NMP, Sigma-Aldrich) solvent was cast onto an aluminum current collector in an Ar-filled glove box, and then dried in a vacuum oven at 80 °C. Other cathode materials and their composite electrodes used in this study, including OV-M85, OV-M86T6, OV-M85A5, and OV-M85T5A5, were also prepared using the same procedure.

Characterization

Sample morphology was examined using a JEOL 7500F field emission SEM instrument at 15 kV. Synchrotron XRD in the transmission mode was performed at beamline 11-3 at Stanford Synchrotron Radiation Lightsource (SSRL) with an X-ray wavelength of 0.974 Å. Raman spectra were collected using a 532 nm Horiba LabRAM Aramis Raman Microscope at the Molecular Foundry (MF) at LBNL. The confocal Raman microscope acquires Raman (80–4000 wavenumbers) and photoluminescence spectra (500–1600 nm) at single points or within 2- and 3-dimensional volumes. XPS data were collected using a Thermo-Fisher K-Alpha Plus XPS/UPS instrument at the MF, equipped with a monochromatic Al Kα X-ray source (1.486 KeV).

For hard XAS analysis, XANES spectra were collected at the SSRL beamline 4-3. Recovered electrode samples, sealed with polyimide tape, were positioned at a 45° angle to the incident X-ray beam. A Si (220) crystal was used as a monochromator, with monochromatic energy calibration achieved using the E_0 value of 6539 eV for a Mn metal foil reference. Data processing was performed using the Demeter package software. Reference electrodes of MnO for Mn(II), Mn_3O_4 for Mn(II/III), Mn_2O_3 for Mn(III), and MnO_2 for Mn(IV) were used as standards. Soft XAS measurements were conducted at the SSRL beamline 8-2. Samples were attached to conductive carbon tapes, which were mounted on an aluminum sample holder rod within an Ar-filled glovebox. Spectral measurements utilized the bending magnet source (4.0 mrad) with a 6 m spherical grating monochromator and a 0.1 mm^2 beam spot. XAS profiles were collected under ultrahigh vacuum (10^{-9} Torr).

Electrochemical measurements

The 2032-type coin-cell half-cells were assembled with 1 M lithium hexafluorophosphate ($LiPF_6$) in 1 : 1 (v/v) of ethylene carbonate (EC): diethyl carbonate (DEC) electrolyte (PuriEL, Soulbrain) and a polypropylene membrane (PP, Celgard 2500) separator. Lithium foil (Alfa Aesar) was used as the counter and reference electrodes. The electrochemical measurements were conducted at a constant current density of 30 mA g^{-1} in various voltage windows as specified. For the CCCV experiments, a 5-hour hold was applied at the top of charge at 4.6 V. The electrochemical data were acquired using a VMP3 battery potentiostat (Bio-Logic Science) at room temperature or 50 °C. All charge and discharge capacities were calculated based on the net active material loading on the electrode. After cycling, the cathode electrodes were extracted from the coin cells and gently rinsed with dimethyl carbonate (DMC) to remove residual electrolyte before analysis.

Custom-built Swagelok cells with inlet and outlet capillaries for gas flow were used for DEMS measurements, as described in previous studies.[59,60] In an Ar-filled glovebox, the cells were assembled with a Li foil anode (FMC), a quartz microfiber separator (Whatman), and a DRX cathode. For each DEMS experiment, 80 μL of 1.5 M $LiPF_6$ in EC (Gotion) was used. A 316 stainless steel mesh disc and a 316 stainless steel ring were placed above the cathode to create a headspace (~100 μL) for gas accumulation. Once assembled, the Swagelok cells were attached to the DEMS system, and the pressure was monitored for 10 minutes to ensure no leaks. Every 10 minutes, a small (500 μL) pulse of Ar (Linde 99.999%) purged the cell headspace and was sent to the mass spectrometer (MS) gas analyzer. MS signals were calibrated for O_2 (Linde 99.999%) in Ar carrier gas to allow for gas quantification. Cells were cycled between 4.6 and 2.0 V at a current of 0.1 mol Li h^{-1} using a Bio-Logic VSP-series potentiostat. For the DEMS experiments at ET, the DEMS cells were placed in a gravity convection oven (MTI) with a small opening at the top, where the cells were attached to the DEMS system. Thermocouple measurements show the cell temperatures were held at 49.0 °C ± 1.0 °C.

Conclusions

In this study, a d^0-TM-free Mn-based DRX oxyfluoride with oxygen vacancies was synthesized to investigate how various material properties and processes influence the DRX-to-δ phase transformation. The findings reveal that activation of tetrahedral sites—a key step for δ-phase formation—is promoted by the combined effects of lithium and oxygen vacancies, oxygen activation, and Mn migration. To accelerate the δ-phase transformation in OV-M90, optimized protocols were developed, enabling rapid activation within a single cycle

using a CCCV method at 50 °C. Conversely, the incorporation of d^0 TMs suppresses δ-phase transformation but greatly improves the cycling stability of δ-activated DRX. We show that the Ti and Al co-doped variant (OV-M85T5A5) delivers exceptional cycling performance, maintaining nearly 100% capacity retention after 100 cycles at 30 mA g^{-1}. Overall, our findings provide fundamental insights into the mechanisms underlying the DRX-to-δ transformation and highlight the intricate balance between phase transition kinetics and cycling durability. The strategies developed, including vacancy engineering, controlled activation protocols, and targeted cation doping, offer a versatile toolkit for optimizing both the performance and longevity of DRX cathode materials, laying the groundwork for the design and development of advanced cathodes for next-generation lithium-ion batteries.

Conflicts of interest

There are no conflicts to declare.

Data availability

The data supporting this article have been included as part of the supplementary information (SI). Supplementary information is available. The SI includes additional XRD, XAS, XPS, Raman, electrochemcial (dQ/dV, cycling protocols), and DEMS data, along with supplementary figures and tables. See DOI: https://doi.org/10.1039/d6eb00038j.

References

1 E. Lee, D. H. Lee, S. Bessette, S. W. Park, N. Brodusch, G. Lazaris, H. Kim, R. Malik, R. Gauvin, D. H. Seo and J. Lee, *Energy Environ. Sci.*, 2024, **17**, 3753.

2 D. Chen, J. Ahn and G. Chen, *ACS Energy Lett.*, 2021, **6**, 1358.

3 H. Li, R. Fong, M. Woo, H. Ahmed, D. H. Seo, R. Malik and J. Lee, *Joule*, 2022, **6**, 53.

4 R. J. Clément, Z. Lun and G. Ceder, *Energy Environ. Sci.*, 2020, **13**, 345.

5 J. Huang, P. Zhong, Y. Ha, Z. Lun, Y. Tian, M. Balasubramanian, W. Yang and G. Ceder, *Small Struct.*, 2023, **4**, 220034.

6 P. M. Csernica, S. S. Kalirai, W. E. Gent, K. Lim, Y. S. Yu, Y. Liu, S. J. Ahn, E. Kaeli, X. Xu, K. H. Stone, A. F. Marshall, R. Sinclair, D. A. Shapiro, M. F. Toney and W. C. Chueh, *Nat. Energy*, 2021, **6**, 642.

7 M. Freire, N. V. Kosova, C. Jordy, D. Chateigner, O. I. Lebedev, A. Maignan and V. Pralong, *Nat. Mater.*, 2016, **15**, 173.

8 L. Li, Z. Lun, D. Chen, Y. Yue, W. Tong, G. Chen, G. Ceder and C. Wang, *Adv. Funct. Mater.*, 2021, **31**, 2101888.

9 L. Li, J. Ahn, Y. Yue, W. Tong, G. Chen and C. Wang, *Adv. Mater.*, 2022, **34**, 2106256.

10 R. Giovine, E. Yoshida, V. C. Wu, Y. Ji, M. J. Crafton, B. D. McCloskey and R. J. Clément, *Chem. Mater.*, 2024, **36**, 3643.

11 N. J. Szymanski, Y. Zeng, T. Bennett, S. Patil, J. K. Keum, E. C. Self, J. Bai, Z. Cai, R. Giovine, B. Ouyang, F. Wang, C. J. Bartel, R. J. Clément, W. Tong, J. Nanda and G. Ceder, *Chem. Mater.*, 2022, **34**, 7015.

12 Z. Yu, Q. Lu, Y. Wang, K. Yu, H. Li, X. Yang, Y. Cheng, F. Xu and L. Sun, *Appl. Surf. Sci.*, 2023, **619**, 156683.

13 J. Ahn, R. Giovine, V. C. Wu, K. P. Koirala, C. Wang, R. J. Clément and G. Chen, *Adv. Energy Mater.*, 2023, **13**, 2300221.

14 Z. Lun, B. Ouyang, D. A. Kitchaev, R. J. Clément, J. K. Papp, M. Balasubramanian, Y. Tian, T. Lei, T. Shi, B. D. McCloskey, J. Lee and G. Ceder, *Adv. Energy Mater.*, 2019, **9**, 1802959.

15 J. Ahn, Y. Ha, R. Satish, R. Giovine, L. Li, J. Liu, C. Wang, R. J. Clement, R. Kostecki, W. Yang and G. Chen, *Adv. Energy Mater.*, 2022, **12**, 2200426.

16 J. Ahn, D. Chen and G. Chen, *Adv. Energy Mater.*, 2020, **10**, 2001671.

17 Z. Cai, B. Ouyang, H. M. Hau, T. Chen, R. Giovine, K. P. Koirala, L. Li, H. Ji, Y. Ha, Y. Sun, J. Huang, Y. Chen, V. Wu, W. Yang, C. Wang, R. J. Clément, Z. Lun and G. Ceder, *Nat. Energy*, 2024, **9**, 27.

18 W. Hua, S. Wang, M. Knapp, S. J. Leake, A. Senyshyn, C. Richter, M. Yavuz, J. R. Binder, C. P. Grey, H. Ehrenberg, S. Indris and B. Schwarz, *Nat. Commun.*, 2019, **10**, 5365.

19 C. H. Shen, S. Y. Shen, F. Fu, C. G. Shi, H. Y. Zhang, M. J. Pierre, H. Su, Q. Wang, B. Bin Xu, L. Huang, J. T. Li and S. G. Sun, *J. Mater. Chem. A*, 2015, **3**, 12220.

20 Y. Fang, J. Zhao, Y. Su, J. Dong, Y. Lu, N. Li, H. Wang, F. Wu and L. Chen, *Energy Mater. Adv.*, 2024, **5**, 0115.

21 Y. Huang, Y. Dong, S. Li, J. Lee, C. Wang, Z. Zhu, W. Xue, Y. Li and J. Li, *Adv. Energy Mater.*, 2021, **11**, 2000997.

22 H. M. Hau, T. Mishra, C. Ophus, T. Y. Huang, K. Bustilo, Y. Sun, X. Yang, T. Holstun, X. Zhao, S. Wang, Y. Ha, G. H. Lee, C. Song, J. Turner, J. Bai, L. Ma, K. Chen, F. Wang, W. Yang, B. D. McCloskey, Z. Cai and G. Ceder, *Nat. Nanotechnol.*, 2024, **19**, 1831.

23 T. Li, Y. Mao, X. Liu, W. Wang, Y. Li, Y. Xiao, X. Hao, T. Zhu, J. You and J. Zang, *Appl. Surf. Sci.*, 2024, **657**, 159841.

24 T. Holstun, T. P. Mishra, L. Huang, H. M. Hau, S. Anand, X. Yang, C. Ophus, K. Bustillo, L. Ma, S. Ehrlich and G. Ceder, *Adv. Mater.*, 2024, 2412871.

25 T. Li, T. S. Geraci, K. P. Koirala, A. Zohar, E. N. Bassey, P. A. Chater, C. Wang, A. Navrotsky and R. J. Clément, *J. Am. Chem. Soc.*, 2024, **146**, 24296.

26 Y. Guo, Y. Yu, P. Ning and J. Chen, *J. Alloys Compd.*, 2024, **1005**, 176000.

27 W. Xu, H. Li, Y. Zheng, W. Lei, Z. Wang, Y. Cheng, R. Qi, H. Peng, H. Lin, F. Yue and R. Huang, *Nanomaterials*, 2021, **11**, 1.

28 Y. H. Zhang, S. Zhang, N. Hu, Y. Liu, J. Ma, P. Han, Z. Hu, X. Wang and G. Cui, *Chem. Soc. Rev.*, 2024, **53**, 3302.

29 F. Zeng, Y. Zhang, Z. Shao, Z. Li and S. Dai, *Ionics*, 2021, **27**, 3739.

30 O. V. Merkulov, I. V. Shamsutov, M. A. Ryzhkov, B. V. Politov, I. V. Baklanova, E. V. Chulkov and V. P. Zhukov, *J. Solid State Chem.*, 2023, **326**, 124231.

31 L. Croguennec, P. Deniard, R. Breca and A. Lecerfb, Nature of the Stacking Faults in Orthorhombic LiMnO$_2$, *J. Mater. Chem.*, 2012, **48**, 24959.

32 D. H. Kwon, J. Lee, N. Artrith, H. Kim, L. Wu, Z. Lun, Y. Tian, Y. Zhu and G. Ceder, *Cell Rep. Phys. Sci.*, 2020, **1**, 100187.

33 P. Kupracz, K. Grochowska, J. Karczewski, J. Wawrzyniak and K. Siuzdak, *Materials*, 2020, **13**, 4019.

34 Z. Hao, J. Lyu, M. Tian, X. Zhang, K. Wang, S. W. Yang, Y. Zhang and G. Q. Xu, *Small Struct.*, 2024, **5**, 2300442.

35 S. Tiwari, N. Balasubramanian, S. Biring and S. Sen, in *IOP Conf Ser Mater Sci Eng*, Institute Of Physics Publishing, 2018.

36 V. C. Wu, H. A. Evans, R. Giovine, M. B. Preefer, J. Ong, E. Yoshida, P. E. Cabelguen and R. J. Clément, *Adv. Energy Mater.*, 2023, **13**, 2203860.

37 K. V. Mishchenko, M. A. Kirsanova, A. B. Slobodyuk, A. A. Krinitsyna and N. V. Kosova, *Chim. Techno Acta*, 2022, **9**, 20229310.

38 D. Chen, J. Zhang, Z. Jiang, C. Wei, J. Burns, L. Li, C. Wang, K. Persson, Y. Liu and G. Chen, *Chem. Mater.*, 2021, **33**, 7028.

39 M. J. W. Ogley, A. S. Menon, B. J. Johnston, G. Pandey, I. McClelland, X. Shi, S. Agrestini, V. Celorrio, G. E. Pérez, S. G. Booth, J. Cabana, S. A. Cussen and L. F. J. Piper, *ACS Energy Lett.*, 2024, **9**, 4607.

40 H. M. Hau, T. Holstun, E. Lee, B. L. D. Rinkel, T. P. Mishra, M. Markuson DiPrince, R. S. Mohanakrishnan, E. C. Self, K. A. Persson, B. D. McCloskey and G. Ceder, *Adv. Mater.*, 2025, 2502766.

41 H. M. Hau, T. Mishra, C. Ophus, T. Y. Huang, K. Bustilo, Y. Sun, X. Yang, T. Holstun, X. Zhao, S. Wang, Y. Ha, G. H. Lee, C. Song, J. Turner, J. Bai, L. Ma, K. Chen, F. Wang, W. Yang, B. D. McCloskey, Z. Cai and G. Ceder, *Nat. Nanotechnol.*, 2024, 1831.

42 D. B. Babu, R. N. Ramesha, P. M. Ette, A. K. Nanda Kumar, A. Arulraj and K. Ramesha, *J. Power Sources*, 2019, **436**, 226870.

43 D. Bosubabu, P. M. Ette, A. K. Nanda Kumar, A. Arulraj and K. Ramesha, *ACS Appl. Energy Mater.*, 2020, **3**, 8716.

44 B. Li, Z. Zhuo, L. Zhang, A. Iadecola, X. Gao, J. Guo, W. Yang, A. V. Morozov, A. M. Abakumov and J. M. Tarascon, *Nat. Mater.*, 2023, **22**, 1370.

45 N. Li, J. Wu, S. Hwang, J. K. Papp, W. H. Kan, L. Zhang, C. Zhu, B. D. McCloskey, W. Yang and W. Tong, *ACS Energy Lett.*, 2020, **5**, 3535.

46 X. Chen, N. Li, E. Kedzie, B. D. McCloskey, H. Tang and W. Tong, *J. Electrochem. Soc.*, 2019, **166**, A4136.

47 L. C. Duda and K. Edström, *J. Electron Spectrosc. Relat. Phenom.*, 2017, **221**, 79.

48 T. Chen, J. Yang, L. Barroso-Luque and G. Ceder, *ACS Energy Lett.*, 2023, **8**, 314.

49 Z. Cai, H. Ji, Y. Ha, J. Liu, D. H. Kwon, Y. Zhang, A. Urban, E. E. Foley, R. Giovine, H. Kim, Z. Lun, T. Y. Huang, G. Zeng, Y. Chen, J. Wang, B. D. McCloskey, M. Balasubramanian, R. J. Clément, W. Yang and G. Ceder, *Matter*, 2021, **4**, 3897.

50 C. Zuo, Z. Hu, R. Qi, J. Liu, Z. Li, J. Lu, C. Dong, K. Yang, W. Huang, C. Chen, Z. Song, S. Song, Y. Yu, J. Zheng and F. Pan, *Adv. Energy Mater.*, 2020, **10**, 2000363.

51 V. C. Wu, P. Zhong, J. Ong, E. Yoshida, A. Kwon, G. Ceder and R. J. Clément, *ACS Energy Lett.*, 2024, **9**, 3027.

52 M. M. Rahman and F. Lin, *Matter*, 2021, **4**, 490.

53 J. Gan, Z. Wu, C. Zheng, F. Qi, C. Li, L. She, Y. Gao, Z. Li, W. Sun, Y. Liu, M. Gao, Y. Jiang, S. He, Y. Yang and H. Pan, *ACS Energy Lett.*, 2024, 6153.

54 N. Voronina and S. T. Myung, *Energy Mater. Adv.*, 2021, **2021**, DOI: 10.34133/2021/9819521.

55 B. Strehle, K. Kleiner, R. Jung, F. Chesneau, M. Mendez, H. A. Gasteiger and M. Piana, *J. Electrochem. Soc.*, 2017, **164**, A400.

56 J. K. Papp, N. Li, L. A. Kaufman, A. J. Naylor, R. Younesi, W. Tong and B. D. McCloskey, *Electrochim. Acta*, 2021, **368**, DOI: 10.1016/j.electacta.2020.137505.

57 Y. K. Sun, C. S. Yoon, C. K. Kim, S. G. Youn, Y. S. Lee, M. Yoshio and I. H. Oh, *J. Mater. Chem.*, 2001, **11**, 2519.

58 B. Deng, H. Nakamura and M. Yoshio, *J. Power Sources*, 2008, **180**, 864.

59 B. D. McCloskey, D. S. Bethune, R. M. Shelby, G. Girishkumar and A. C. Luntz, *J. Phys. Chem. Lett.*, 2011, **2**, 1161.

60 B. D. McCloskey, A. Speidel, R. Scheffler, D. C. Miller, V. Viswanathan, J. S. Hummelshøj, J. K. Nørskov and A. C. Luntz, *J. Phys. Chem. Lett.*, 2012, **3**, 997.